

Localization of turbulent flows by intensity fluctuations of translucent laser radiation

A.L. Afanas'ev, V.A. Banakh, and A.P. Rostov

*Institute of Atmospheric Optics,
Siberian Branch of the Russian Academy of Sciences, Tomsk*

Received March 20, 2008

Wavelet method of spatial filtration of random intensity nonhomogeneities in distribution of intensity of a laser beam, trans-illuminating the turbulent flow, is proposed and experimentally proved. The method allows one to determine the distance to the flow and its velocity.

Introduction

Present-day investigations of wind and temperature field fluctuations in the atmosphere^{1–8} have shown that their spatial structure is determined by simultaneous coexisting turbulent (chaotic) nonhomogeneities and greater quasiordered formations. The presence of areas with the ordered motion is typical for a convective boundary layer, where the exchange processes and the transfer of mechanical and heat energies in the entire boundary layer proceed mainly due to coherent structures.^{3,4,7,8} At the same time, the efficient methods of indication of organized structures and investigation of their evolution are not developed up to now.⁸

In a series of applied problems, an urgent need of determining and visualization of regions with an increased turbulence in the atmosphere has appeared, for example, in development of safety systems for flying apparatus,^{9,10} or in analysis of distortions of wide-panorama long-exposition images.¹¹

Therefore, the necessity became to develop methods of visualization of large-scale quasi-regular structures and regions of increased turbulence; as well as methods of space-limited turbulent flow localization. In this connection, of interest is the investigation of remote indication of regions with increased turbulence based on intensity fluctuations of the translucent optical radiation. This principle lies in the base of methods of estimating the averaged transversal wind velocity along the path of the optical wave propagation, as well as methods of wind profiling.^{12–18} So, the computer simulation has shown^{16–18} that it is possible to retrieve profiles of the transverse wind velocity vector with a high accuracy via statistical processing of time realizations of laser beam images.

This paper describes the experimental investigation of the contribution of turbulent nonhomogeneities, localized at individual parts of the atmospheric path, into total intensity distribution distortions of the beam propagating along this path. Experimentally, finding the contribution of individual path parts into beam distortions was

realized by detecting nonhomogeneities of different scales in the beam intensity and tracing the evolution of these nonhomogeneities. It was assumed that the movement velocity of the intensity nonhomogeneities of a given scale S_Z in the beam cross section depends on the movement velocity of air turbulent nonhomogeneities at the distance Z from the receiver. To separate space scales of the nonhomogeneities, the wavelet analysis was used, whose efficiency in problems of determining typical scales of random fields and indicating coherent structures has been demonstrated in many cases.^{19–24}

Experiment

To study the role of turbulent nonhomogeneities, located at different distances from the receiving plane, in formation of the random space structure of intensity distribution in the cross section of a translucent beam, an artificial local turbulent flow was used, moving along the path. An optical path of 140 m length, free from the turbulence and motion of medium, was located in a closed room. The artificial layer of the turbulent medium, moving across the path, was modeled using a fan heater. The experimental diagram is given in Fig. 1.

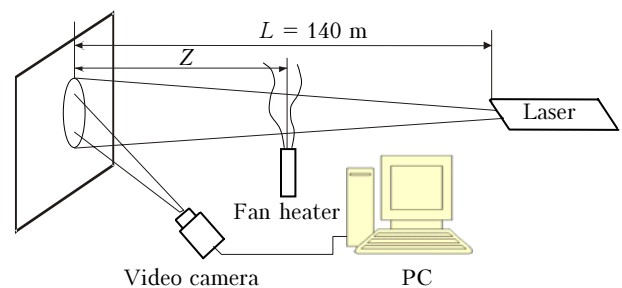


Fig. 1. Schematic view of the experiment.

As an optical source, a solid-state laser with a wavelength of 532 nm and a mean power of 30 mW was used. The beam diameter at the laser output was 0.4 mm and the angular divergence was 1.2 mrad.

The beam diameter at the receiving end of the path was 500 mm (by the level of half power). The fan heater was located at the definite distance Z from the reception plane, at 0.5 m distance from the beam centre. The thermal flow was perpendicular to the beam. The flow velocity was 1.2 m/s at a distance of 0.5 m from the nozzle.

To visualize the intensity distribution in the beam cross section, a screen was located at the path end. The beam image on the screen was recorded by a high-speed video camera (DALSA) with a frame size of 544×512 pixels and a mean velocity of scanning of 212 frames per second. The information from the video camera was recorded as a binary file to the computer hard disk.

Fragments of video-recording represent a classical pattern of the moving shadows. At a slowed reproduction (10 frames per second) it is clearly seen that the spatial nonhomogeneities of the image intensity are shifted, deformed, disappeared, and appeared again, the pattern shifts and changes in accordance with the motion and evolution of the disturbing air flow nonhomogeneities. Over the course of observing several frames, it is possible to trace the movement of individual intensity nonhomogeneities with a characteristic space scale. It is evident that when measuring the average spatial image shifts between neighboring frames and taking into account the beam geometry, at a known frequency of frames it is possible to measure the integral for the path velocity of the turbulent flow motion.

Figure 2 shows the characteristic examples of individual frames obtained at different distances Z between the disturbing turbulent flow and the screen. The main feature of the images is the difference in space scales of nonhomogeneities in the beam cross-section. Evidently, this is due to the geometric divergence of the beam; correspondingly, the projections of the flow turbulent nonhomogeneities to the receiving plane have the dimension proportional to the distance Z .

Another distinctive feature of images in Fig. 2 is different velocities of the pattern motion. Turbulent nonhomogeneities, located far from the receiver, create the fast moving images of large scale on the screen, while those, located closer to the receiver, create slowly moving images with a smaller scale. At the same velocity of the turbulent flow this is evidently caused by the same geometric beam divergence and, correspondingly, by different times of intersecting the beam by the flow nonhomogeneities.

Thus, it can be supposed that there is one-to-one correspondence between the typical scale S_z of the image and the distance Z of the turbulent layer, forming this scale on the screen. Tracing the motion velocity of nonhomogeneities of different scales in the beam image, it is possible to judge about the media motion velocity at one or another distance along the propagation path and to determine the location of turbulent areas (areas of increased turbulence), as well as characteristic velocities of the medium motion in these regions.

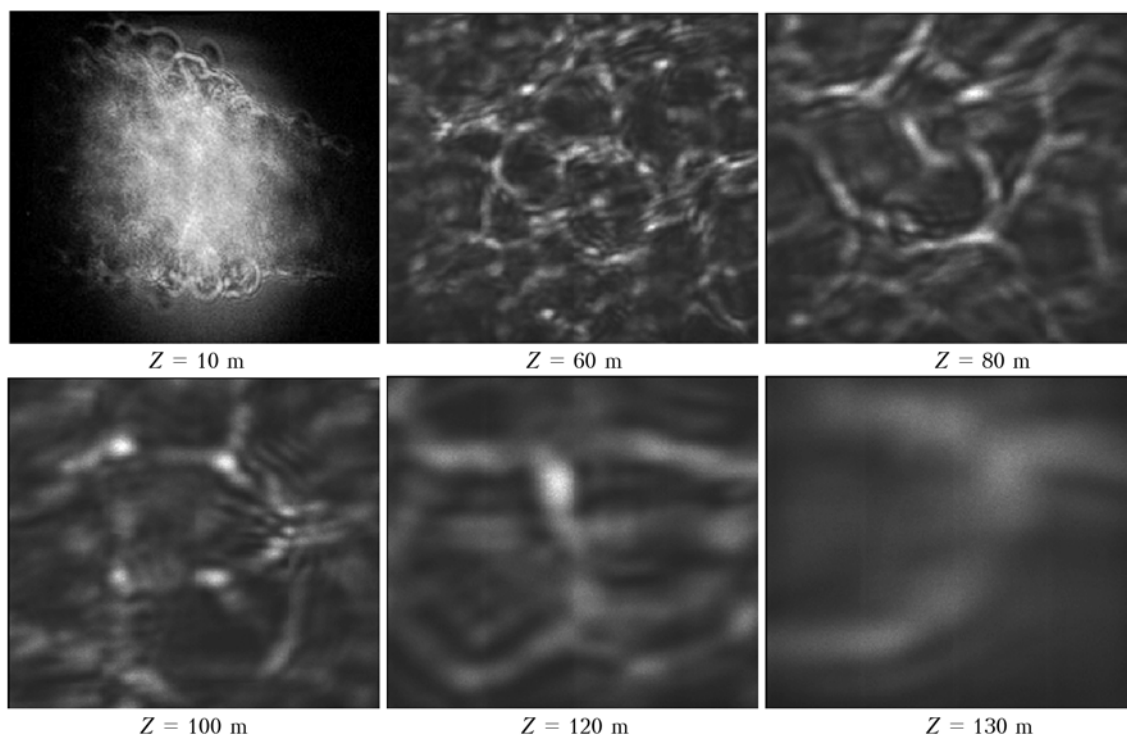


Fig. 2. Individual frames of beam image at different distances Z to the disturbing turbulent flow.

Wavelet analysis of experimental data

Under the assumption on the existence of one-to-one correspondence between the typical scale S_Z of the image and the distance Z from the turbulent layer to the screen, the flow velocity at the distance Z can be written in the form

$$V_Z = k \frac{\Delta R_S}{\tau}, \tag{1}$$

where $k = 1 - Z/L$ is the geometric factor, L is the path length, $\tau = 1/f$, f is the frame frequency, ΔR_S is the spatial inter-frame shift of image nonhomogeneities with the characteristic scale S_Z .

Determine the dependence of the characteristic scale of the image S_Z on the distance Z as $S_Z = F(Z)$. For this purpose, let us analyze the beam images, obtained at different distances Z to the turbulent layer (Fig. 2), with the use of the spatial wavelet-transform. Data series, formed from the brightness values of single pixels on image frames, served as the object of the transformation.

The wavelet-transform function $F(Z)$ is determined as its integral transformation with the kernel $\Phi(\xi)$

$$\Psi(s, \chi) = s^{-1/2} \int_{-\infty}^{\infty} F(x) \Phi\left(\frac{x - \chi}{s}\right) dx, \tag{2}$$

where s is the scale; χ is the shift (spatial in this case); $\Phi(\xi)$ is the wavelet function. The Mexican hat wavelet was used:

$$\Phi(\xi) = (\xi^2 - 1) \exp(-\xi^2 / 2), \tag{3}$$

allowing a sufficiently good recognition of maxima and minima in a signal.

The energy density is distributed in the wavelet-plane as

$$E(s, \chi) = \frac{|\Psi(s, \chi)|^2}{\pi}. \tag{4}$$

The energy distribution can be integrated over χ (time or spatial coordinate) for every scale s

$$E(s) = \int_0^{\infty} E(s, \chi) d\chi. \tag{5}$$

As a result, the energy distribution over scales (frequencies) is obtained like in calculating the Fourier power spectrum. In this case, the frequency localization is not so accurate as in the Fourier transform, when the harmonic signal gives δ -pulse at the signal frequency; however, in the case of the wavelet-transform, the time (spatial, in our case) localization of the frequency (scale) spike is due to the decrease in the frequency resolution. In our case the maximum of $E(s)$ determines the magnitude of the characteristic spatial scale S_Z in the beam image intensity distribution under analysis.

Figure 3 shows the two-dimensional wavelet-transform of a single image frame (in the centre) at different scales S : from the smallest to larger ones.

A similarity with the initial image is observed for all scales, that is, in a given case the wavelet-transform works as a spatial filter separating a given scale in the image. By changing the scale S in the transform (2), a correspondence with the characteristic scale of a particular image can be reached.

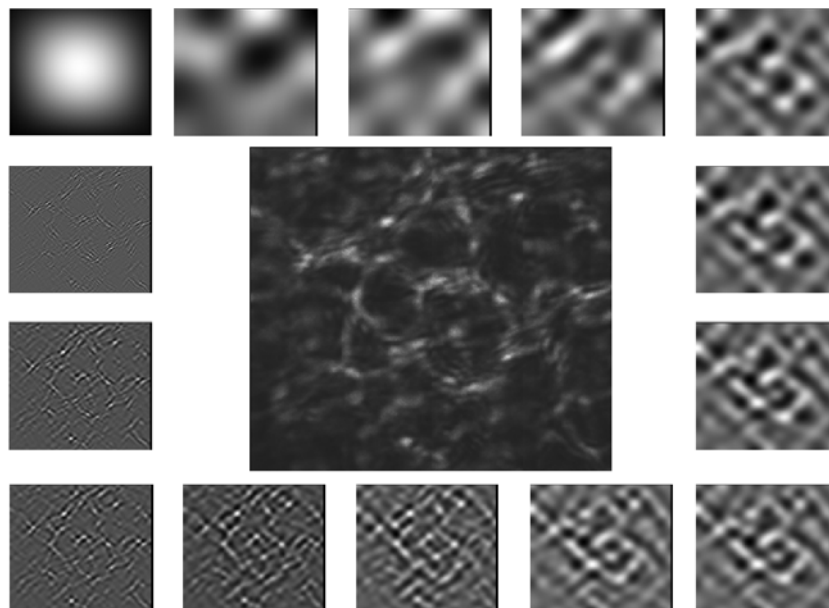


Fig. 3. An example of two-dimensional wavelet-transforms of a single frame of the image at different scales.

In figure 3, due to the peculiarities of visualization (the normalization at every scale was made to its maximum in order to obtain the maximal image contrast), the differences in the amplitude (brightness) between the filtered images is not seen. In fact, the amplitudes of wavelet coefficients differ greatly for different scales. In each specific case the amplitude of coefficients is maximal at a definite scale, when the "filtered" image becomes the most contrast. This scale just is the characteristic scale of the initial image.

Figure 4 shows a more traditional representation of the plane of wavelet-coefficients for three cases of the turbulent layer locations. As an input one-dimensional data array $F(x)$ for transform (2), the line, averaged over columns of a single frame image, is taken here. The spatial coordinate is plotted along the image line in pixels is plotted on the abscissa, and the scale (in mm) is plotted on the Y-axis. The successive change of frames gives an idea of the dynamics of spatial localization of wavelet-coefficients over all scales. First, it is seen that for each distance its own scale is predominant, and, second, the velocity of this scale movement is proportional to the distance.

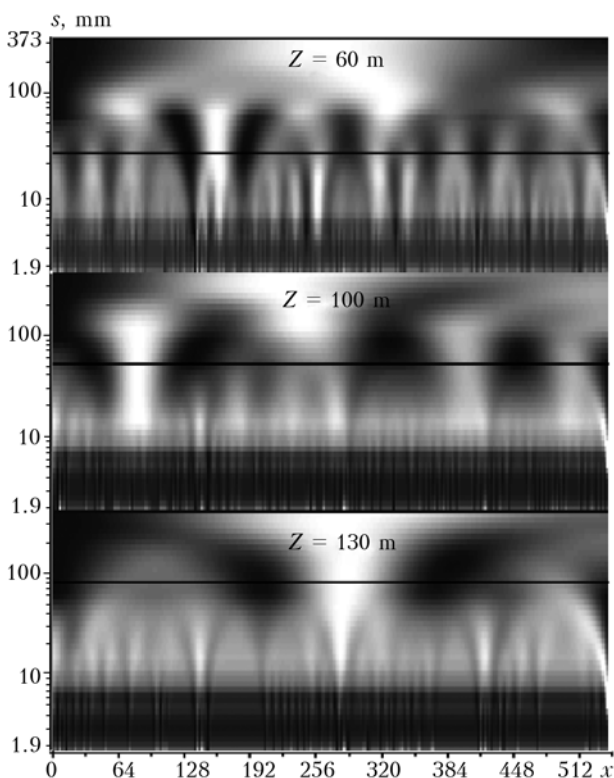


Fig. 4. The plane of wavelet-coefficients of an averaged image line for three cases of the turbulent layer location.

To underline maximally spatial variations for each scale, the contrast visualization in Fig. 4 was realized by normalization not on the maximal value of amplitude among the plane of wavelet-coefficients,

but at a constant scale – on the maximal amplitude of the coefficient in a line. The drawback of such visualization is the fact that, on the one hand, there are sharp vertical changes of intensity of the gray, and, on the other hand, the images of individual adjacent signal components can merge with each other, although in fact they have different amplitude. The energy density (4) and the power spectrum (5) were calculated further based on the calculated distribution of wavelet coefficients $\Psi(S, x)$.

In the course of experimental data processing the frequency-spatial distributions of wavelet coefficients and wavelet spectra for every line of the initial image were calculated. Then the spectra were averaged over all lines. A characteristic scale of intensity nonhomogeneities for a given frame was determined by the position of maximum of the averaged spectrum. The characteristic scale S_Z of the image for the distance Z of the turbulent flow position was estimated as the result of averaging over 100 successive frames (~ 0.4 s).

Figure 5 shows the averaged power spectra obtained in the experiment for different distances.

The maxima of spectra in the range of large scales are stipulated by the initial distribution of the beam intensity. The spectral maxima are informative in the range of small scales. Their positions correspond to the characteristic spatial scales, which are accounted for the maximal power of spatial signal fluctuations (intensity in the averaged line of beam image at one or another distance to the turbulent layer).

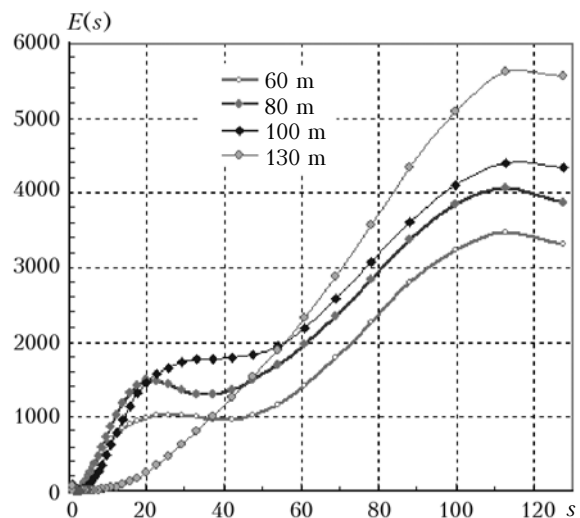


Fig. 5. Averaged wavelet spectra of power.

Figure 6 shows the experimentally determined distance dependence of the characteristic scale S_Z (in pixels). As it was noted above, the growth of a characteristic scale of the intensity spatial nonhomogeneities in the image at the increase of the distance between the turbulent flow and the screen should be linear and determined by the geometric

beam divergence. However, in fact, the experimental dependence is of nonlinear character, and a faster growth of scales, than it follows from geometric constructions, occurs with the distance increase.

The thing is that as the beam narrows approaching to the source, the more and more increasing projections of the lesser an lesser medium nonhomogeneities begin to dominate in formation of random intensity distribution in the beam image on the screen, thus decreasing the relative contribution of small nonhomogeneities of intensity to the formation of the characteristic scale S_z . In the limiting case, at a distance of 130 m, the single maximum remains in the spectrum in the region of large scales, i.e., the characteristic scale S_z , in fact, coincides with the "projection" to the screen of the initial beam.

Then two-dimensional wavelet-transforms of all frames of the initial image have been performed sequentially at different scales S_z , thus forming the images at these scales. According to the curve in Fig. 6, the inter-frame shifts of each filtered image correspond to shifts of optical nonhomogeneities of the medium at particular distances, and the flow velocity at these distances can be estimated by formula (1).

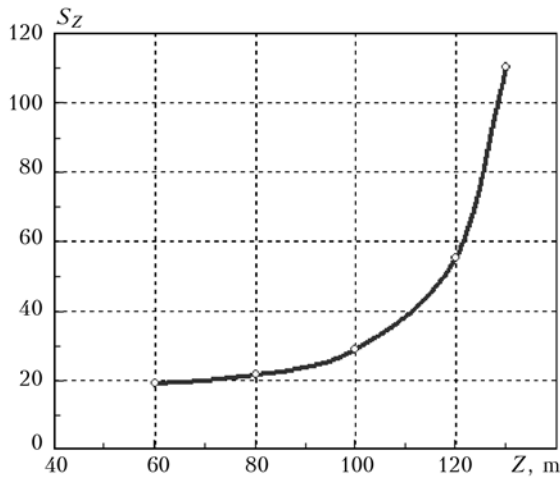


Fig. 6. Typical scale of image as a function of the distance to the turbulent flow.

To determine the space shift ΔR_s of the inter-frame correlation of images, the Fourier analysis of image lines was used. As an example, figure 7a shows the intensity distributions of an averaged line for two neighboring frames of an unfiltered initial image for the case, when the fan heater is 60 m away from the screen. Figure 7b shows their cross-correlation function. The spatial shift of the maximum is clearly seen as well.

For these two frames, figure 8a shows the averaged image lines filtered at a typical scale $S_z = 13.9$ mm. The cross-correlation of the filtered frames (Fig. 8b) has the same shift of the maximum.

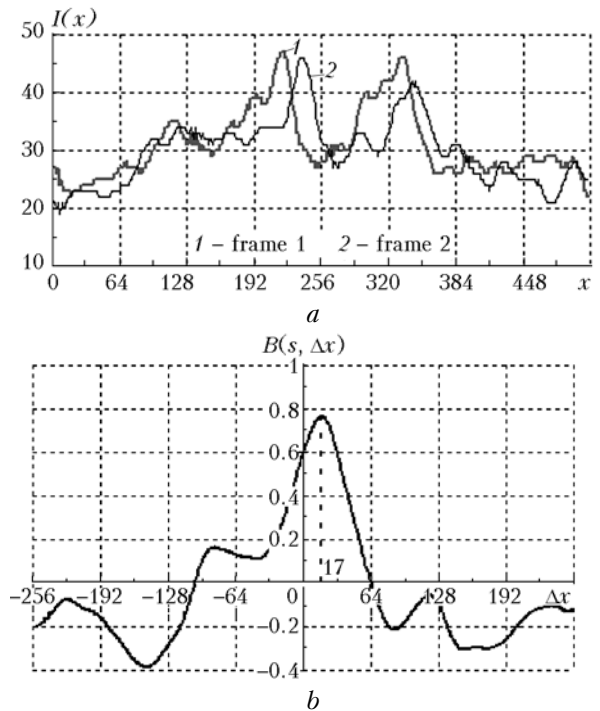


Fig. 7. Intensity distributions in the averaged line for two neighboring frames of unfiltered initial image (a). Cross-correlation function for intensities (b).

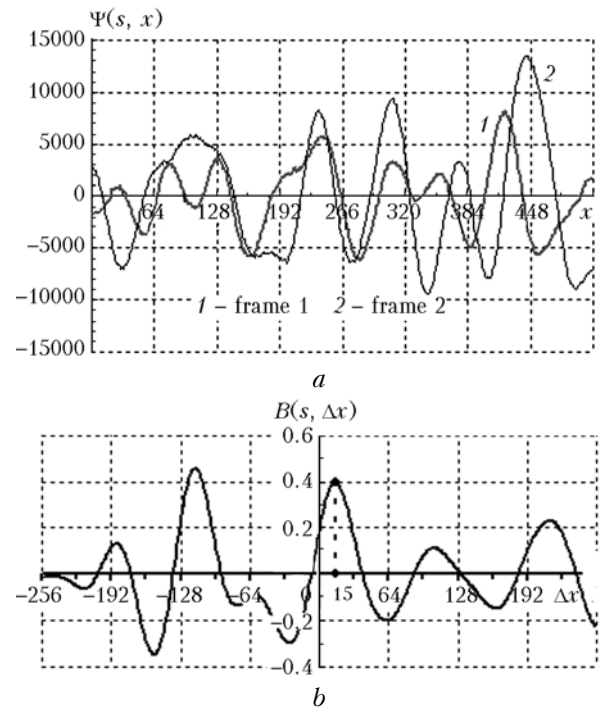


Fig. 8. Averaged image lines filtered at the characteristic scale S_z (a). Inter-frame cross-correlation function for lines of the filtered image (b).

Figure 9 shows data for the same frames of the initial image, but filtered at the scale, approximately twice differing from the typical one. It is seen that the amplitude of the wavelet coefficients decreased

more than two-fold as compared with the amplitude of wavelet coefficients at a characteristic scale.

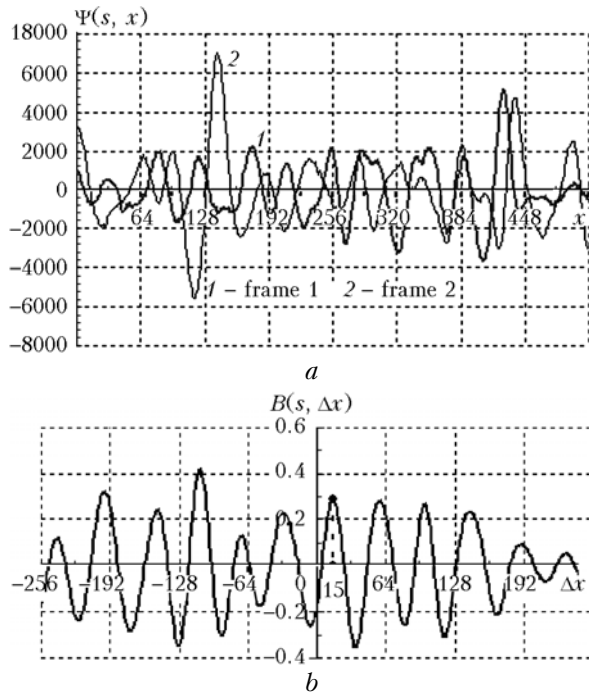


Fig. 9. Averaged lines of image filtered at the scale differed from the characteristic one (a). Inter-frame cross-correlation function for lines of the filtered image (b).

The cross-correlation in the maximum also decreased, although the shift remained the same as in Figs. 7 and 8, because the distance is the same. Thus, incorrect localization of the turbulent flow with the use of filtration at the scale, differed from the characteristic one, leads to the decrease of the amplitude of wavelet coefficients. Moreover, incorrect determination of the distance results in evident incorrect estimates of the air motion velocity in the turbulent flow.

Actually, an error in determination of the distance to the flow, for example, its underestimating (the wavelet filtration is realized at a lesser scale than the characteristic one) will result in the increase of the coefficient k in Eq. (1), and independently estimated velocity of the inter-frame shift and the spatial shift of maximum ΔR_S will correspond to a greater distance, and, hence, their values will be larger than they should be for underestimated distance. As a result, the velocity, estimated by Eq. (1) for the underestimated distance, will be improbably large. Such wrong cases can be easily rejected during the processing and will not worsen the accuracy of localization of turbulent areas.

Based on the obtained successions of inter-frame shifts ΔR_S of images, filtered at characteristic scales using Eq. (1), the values of the turbulent flow velocity at distances Z were calculated. Figure 10 shows the estimates of time series of the velocity for different distances of the flow location.

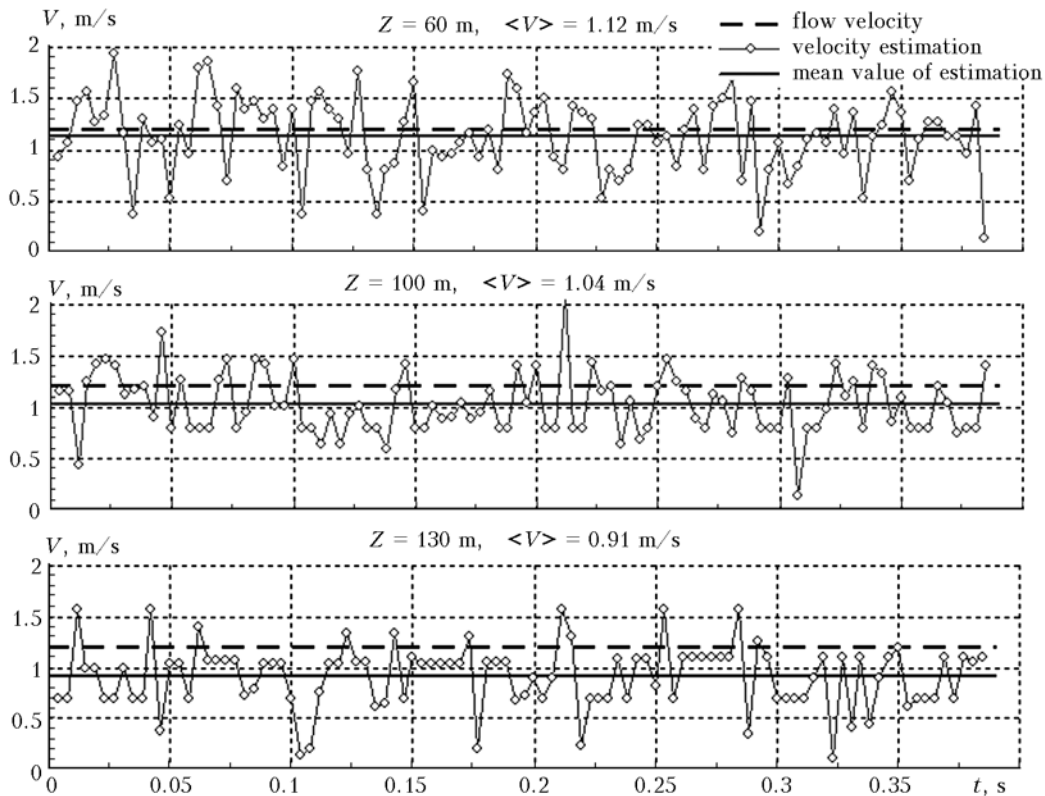


Fig. 10. Estimations of the velocity of the artificial local turbulent flow at different distances Z of its location on the path.

The measured value of the velocity of artificial local turbulent flow created by the fan heater is shown by a dashed curve. The solid curve shows the mean value of the velocity estimate by the proposed methods. It is evident that although the accuracy of determination of the velocity decreases with the increase of the distance to the screen, the obtained estimates agree with the measured values within the permissible error.

Conclusion

The developed method allows one to determine the location of turbulized areas along the path of a translucent optical beam propagation and to evaluate the velocity of medium motion in these areas.

Acknowledgements

This work was supported by the Russian Foundation for Basic Research (Projects Nos. 06-05-64445 and 060596951).

References

1. N.Z. Pinus, *Izv. Akad. Nauk SSSR, Fiz. Atmos. i Okeana* **24**, No. 1, 3–8 (1988).
2. N.Z. Pinus and G.H. Shur, *Meteorol. Gidrol.*, No. 4, 19–24 (1989).
3. A.G. Williams and J.M. Hacker, *Boundary-Layer Meteorol.* **34**, 55–74 (1993).
4. E.J. Plate, E.E. Fedorovich, D.X. Viegas, and J.C. Wyngaard, eds., *Booyant Convection in Geophysical Flows*, NATO ASI Series, Vol. 513 (Kluwer Academic Publishers, 1998), 491 pp.
5. G.N. Shur, *Meteorol. Gidrol.*, No. 1, 5–11 (1994).
6. G.N. Shur, *Meteorol. Gidrol.*, No. 1, 50–57 (1997).
7. I.V. Petenko and V.A. Bezverkhni, *Meteorol. Atmos. Phys.* **71**, 105–116 (1999).
8. V.N. Ivanov and N.L. Byzova, *Meteorol. Gidrol.*, No. 1, 5–25 (2001).
9. V.A. Banakh, Ch. Werner, and I.N. Smalikho, *Atmos. Oceanic Opt.* **14**, No. 10, 856–863 (2001).
10. T. Halldorsson, A. Langmeier, A. Prucklmeier, V.A. Banakh, and A.V. Falits, *Proc. SPIE* **6522**, 65220A-1–65220A-9 (2006).
11. D. Fraser, G. Thorpe, and A. Lambert, *J. Opt. Soc. Am. A* **16**, No. 7, 1751–1757 (1999).
12. Wang Ting-I, G.R. Ochs, and S. Lawrence, *Appl. Opt.* **20**, 4073–4081 (1981).
13. S.F. Clifford, G.R. Ochs, and Wang Ting-I, *Appl. Opt.* **14**, No. 12, 2844–2850 (1975).
14. J.F. Holmes, M.H. Lee, and M.E. Fossey, *J. Opt. Soc. Am. A* **70**, 1586 (1980).
15. R. Johnston, C. Dainty, N. Wooder, and R. Lane, *Appl. Opt.* **41**, 6768–6772 (2002).
16. V.A. Banakh and D.A. Marakasov, *J. Opt. Soc. Am. A* **24**, No. 20, 3245–3254 (2007).
17. V.A. Banakh, D.A. Marakasov, and M.A. Vorontsov, *Appl. Opt.* **46**, No. 33, 8104–8117 (2007).
18. V.A. Banakh and D.A. Marakasov, *Opt. Lett.* **32**, No. 15, 2236–2238 (2007).
19. E.L. Andreas and G. Trevino, *J. Atmos. Ocean. Technol.* **14**, 554–564 (1997).
20. J.M. Rees, W.J. Staszewski, and J.R. Winkler, *Dyn. Atmos. Oceans* **34**, 245–261 (2001).
21. I.V. Petenko, *Boundary-Layer Meteorol.* **100**, 287–299 (2001).
22. S.M. Shmeter, A.A. Postnov, and G.N. Shur, *Meteorol. Gidrol.*, No. 3, 25–37 (2003).
23. G.N. Shur, B.N. Lepukhov, and L.A. Sokolov, *Meteorol. Gidrol.*, No. 5, 54–61 (2003).
24. A.L. Afanas'ev and V.A. Banakh, *Atmos. Oceanic Opt.* **19**, No. 7, 540–546 (2006).